PHYSICAL REVIEW B VOLUME 17, NUMBER 12 15 JUNE 1978

Raman scattering from condensed argon

R. K. Crawford
Department of Physics and Materials Research Laboratory, University of Illinois, Urbana, Illinois 61801 and Solid State Science Division, Argonne National Laboratory, Argonne, Illinois 60439

D. G. Bruns, D. A. Gallagher, and M. V. Klein
Department of Physics and Materials Research Laboratory, University of Illinois, Urbana, Illinois 61801
(Received 7 September 1977)

Two-phonon Raman spectra have been measured for solid-argon samples at two densities at low temperature. These results are compared with published calculations based on a point-dipole model, and some shortcomings of this model are indicated. The development of the Raman spectra with increasing temperature in the solid at constant density has been studied, and the results discussed in the context of this model. Finally, spectra were measured for solid and fluid argon at a number of points along the melting curve at pressures up to 4 kbar, in order to explore the changes which occur upon melting. These results are compared with previously published data for fluid argon at other temperatures and pressures. Some comparisons with molecular-dynamics calculations are also made.

I. INTRODUCTION

Second-order ("two-phonon") Raman-scattering spectra in principle contain a wealth of information, both about the short-time dynamics of a system and about the deformations which the charge distributions undergo during these dynamical processes. Unfortunately, because of the way this information is folded together, experimental spectra (except those for dilute gases) have proven extremely difficult to interpret, although some progress has been made for spectra from solid alkali halides[1] and tetrahedrally bonded covalent materials.[2] The condensed noble gases have closed-shell electronic configurations and their dynamics have been extensively studied both experimentally and theoretically. For these reasons these systems offer perhaps the greatest chance of success for unraveling the various contributions to the Raman spectra. In recent years spectra have been measured in the liquid and solid noble gases and several attempts have been made to calculate the spectral shapes and intensities. The present experiments were undertaken to provide spectra for quantitative comparison with theory at low temperature as well as to extend the density and temperature range over which experimental spectra for solid and fluid were available.

II. EXPERIMENTAL

The samples were contained inside a beryllium-copper pressure vessel shown in Fig. 1. This vessel was constructed to fit inside a Janis Super Vari-Temp cryostat. Platinum and germanium resistance thermometers were mounted at the top of the vessel for temperature measurement and control. No attempt was made to achieve accuracy better than about one degree. Temperature was controlled by varying the current through a heater on the vessel, using a proportional controller operating on the signal from the measuring thermometer. A separate manually controlled heater on the vessel was used to adjust the gradient along the sample. A third heater was wound around the pressure tubing to keep it from blocking during sample growth.

The light-scattering geometry used is indicated in the inset in Fig. 1. Because of space limitations it was not feasible to construct an optical window for the laser beam to exit from the top of the vessel. Instead, the incident beam was reflected 180° by a mirror surface above the scattering region inside the vessel, so the beam passed back through the scattering region and out the bottom window of the vessel. This arrangement has the added advantage of effectively doubling the scattering volume, although this advantage is partially offset by the increase in stray light scattered from the vessel walls. All windows had internal masks to reduce the effects of stray scattered light as much as possible. For construction purposes, a third window was located opposite the scattered-light exit window. In operation, this third window transmitted scattered light to an external absorber, providing an effectively "black" wall behind the scattering volume.

The pressure vessel windows were single-crystal sapphires (0.635 cm diam. $\times$0.318 cm thick) with the c axis normal to the window flats. On initial assembly, thin indium foils were placed between the windows and the seats machined inside the vessel. A gentle push on the insides of the

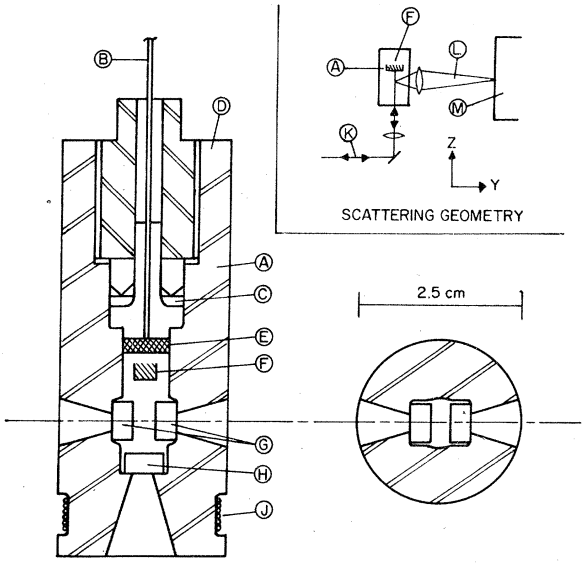

FIG. 1. High-pressure cell for Raman scattering. A—cell body; B—pressure tubing; C—pressure seal; D—thermometer block attached here; E—gas filter; F—mirror (supports not shown); G—exit windows for scattered light; H—entrance and exit window for laser beam; J—heater. Inset: A—pressure cell (cryostat around cell is not shown); F—mirror; K—laser beam; L—scattered light; M—monochromator.

windows then served to provide an initial seal. A spring assembly inside the pressure vessel exerted sufficient force on the windows to keep them in place when the vessel was not pressurized.

Since the sapphire windows were birefringent, polarization analysis was somewhat complicated. Limited attempts to introduce polaroid analyzers inside the pressure cell proved unsuccessful, primarily due to space limitations. However, as the analysis in the Appendix shows, polarization information is not eliminated by the windows, so most spectra were measured with an analyzer in the scattered beam outside the pressure vessel.

The gas pressure was generated using a standard pressure system similar to ones described previously.[3] Initial pressurization of the system was achieved with a two-stage air-driven diaphragm pump, while final pressures were reached by varying the piston displacement in a hydraulic intensifier. Pressures in the fluid phase were measured with a bourdon gauge accurate to 0.2%.

Great care was taken to flush the pressure system thoroughly before introducing a gas sample, but despite these efforts a number of unknown small particles were observed drifting slowly through the liquid samples whenever material was added to or removed from the pressure vessel. These particles were not visible to the naked eye but could easily be observed through the collecting lens using the spectrometer periscope, and were estimated to be up to about 10 μm in size. Subsequent spectroscopic analysis of the gas samples yielded no information about these particles, and their nature and origin was never determined. After a short wait these particles would settle to the bottom of the liquid samples and introduced no difficulty for the liquid measurements. However, whenever solid samples were grown, some of these particles were inevitably trapped in the solid, significantly increasing the amount of light elastically scattered from the sample. Inclusion of a filter inside the vessel did not alleviate the problem.

The preparation of a liquid sample at any desired combination of pressure and temperature was quite straightforward. However, once the vessel was filled with solid, the amount of material in the vessel could not be changed. Since the vessel was essentially rigid, this meant that the solid was constrained to remain at nearly constant density as the temperature was changed. The variation of pressure with temperature along one of these pseudoisochoric paths is determined by the equation of state of the sample and the elastic behavior of the pressure vessel.[4] Samples of various known densities could be prepared by growing the solid at different temperatures along the melting curve[5] (and hence at different initial pressures).

The pseudoisochoric paths followed by the different argon samples studied are shown in Fig. 2. As long as these solids remained at positive pressure the temperatures could be changed rapidly

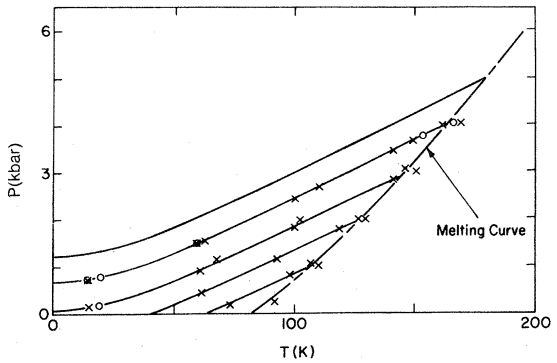

FIG. 2. Pseudoisochoric paths followed by solid-argon samples. × —points at which spectra were measured with original double monchromator system. O-points at which spectra were measured with the triple-monochromator system.

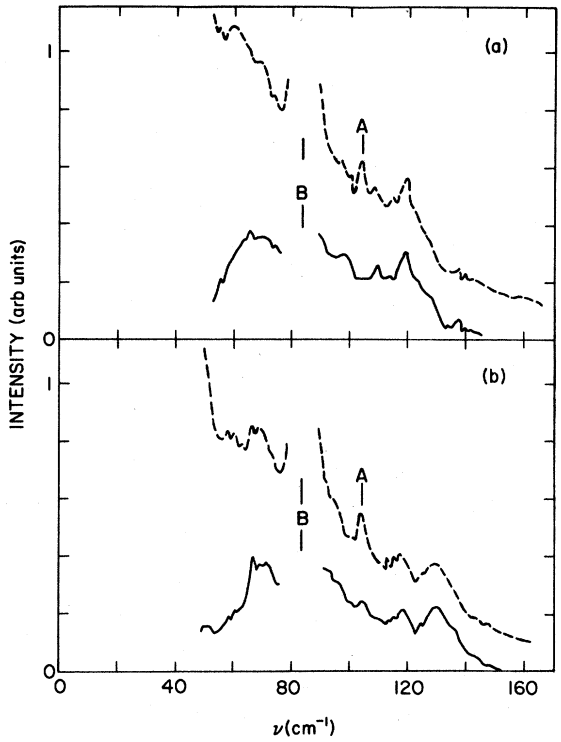

FIG. 3. Typical low-temperature spectra from solid argon measured with double monochromator. (a) 15 K, 22.6 cm^3/mole. Dashed curve are raw data; solid curves are results after background has been subtracted. (b) 15 K, 22.0 cm^3/mole. *B* indicates grating ghost; *A* is laser fluorescence line.

without producing any measurable irreversible effects in the sample. However, only a slight negative pressure was required to fracture the sample, as was observed on several occasions.

Measurements on argon were made during two different periods of time. In the first set of measurements a standard Spex 1400 double monochromator was used with an argon-ion laser. Most spectra were taken with the 4880-Å laser line with about 1 W in this line. The monochromator was equipped with Bausch and Lomb gratings, 1200 lines/mm, blazed at 1 μm, which were used in second order for this experiment. A spectral slit width of 2 cm^{-1} was used. The light elastically scattered, primarily from the small particles referred to above, was fairly intense and the inelastic signal of interest was quite small at low temperatures. This resulted in spectra which were dominated by the incomplete rejection of this elastic light by the monochromator. This "elastic background" could be approximately determined by placing a good elastic scatterer in the sample position. A typical "raw" spectrum from solid argon at low temperatures is shown in Fig. 3 along with the results after the elastic background has been subtracted. A sharp peak in the background near 80 cm^{-1}, which resulted from a grating ghost, prevented a meaningful subtraction in this region. Since the inelastically scattered signal increased rapidly with increasing temperatures, these effects were much less severe at higher temperatures.

In order to obtain better low-temperature spectra, a later set of measurements were made using a different Spex 1400 double monochromator to which a third monochromator stage had been added. This third stage, which was not scanned, was operated with slits wide open and was set to just eliminate the elastically scattered light while passing inelastic signals over the range ~20–250 cm^{-1} away from the laser line. This Spex 1400 double monochromator was equipped with Jobin Yvon gratings, 1200 lines/mm, blazed at 5000 Å, and used in first order for this experiment. The third monochromator stage was equipped with a Bausch and Lomb grating, 1200 lines/mm, blazed at 5000 Å, and used in first order. The double monochromator was operated with 2-cm^{-1} spectral slit width. The 4880-Å argon-ion laser line with about 3 W in this line was used for this set of measurements. With this arrangement the elastic background was made quite small and nearly constant over this range. The marked improvement in signal to noise is evident in the scans shown in Fig. 4, which are for samples under similar conditions to those shown in Fig. 3.

III. LOW-TEMPERATURE RESULTS

Low-temperature spectra ($T < 20$ K) for solid argon at two different densities are shown in Fig. 4. All spectra were obtained with photon counting in a step-scan mode. A counting time of 50 sec/step and a 1-cm^{-1} step were used for these scans. Spectrometer bandpass was approximately 2 cm^{-1}. The shapes of the elastic background for (*XX*) and (*XZ*) configurations of the external polarization analyzer were determined from independent measurements with a good elastic scatterer (loosely pressed powdered MgO), and the background amplitudes were fit to the argon data at small values of ν where scattering from the argon was expected to be negligible. The resulting backgrounds (smoothed) are shown in the figures. The sharp lines at 38 and 103 cm^{-1}, which are fluorescence lines from the argon-ion laser, were not included as part of the background because their amplitudes depended on the precise setting of the laser and hence were not always reproduced.

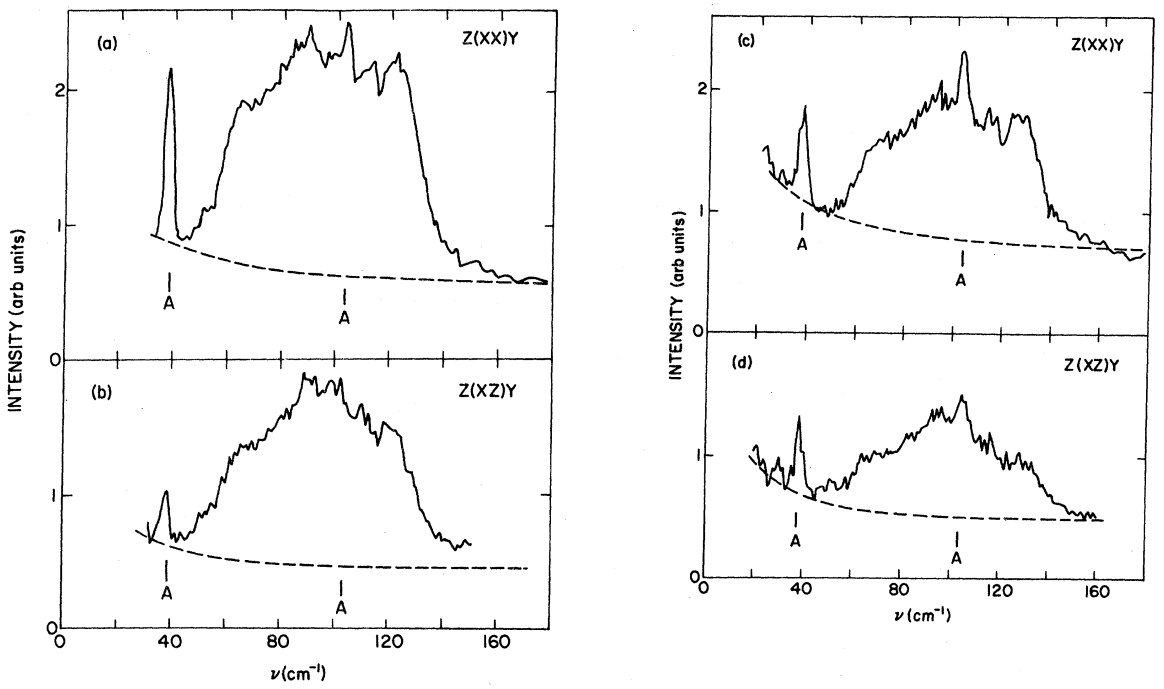

FIG. 4. Raw spectra from solid argon measured with triple monochromator. (a, b) 19 K, 22.6 cm^3/mole; (c, d) 14 K, 22.0 cm^3/mole. Dashed lines show background. *A* indicates laser fluorescence lines.

According to the Appendix, the *X*- and *Z*-polarized components I_{XX}, I_{XZ} of the scattered light inside the pressure vessel are

$$I_{XX} \cong \tfrac{1}{2}(3I'_{XX} - I'_{XZ}), \quad I_{XZ} \cong \tfrac{1}{2}(3I'_{XZ} - I'_{XX}), \qquad (1)$$

where I'_{XX} and I'_{XZ} are just the differences between the measured intensities and the backgrounds in the scans shown in Fig. 4. The resulting I_{XX} and I_{XZ} spectra are shown in Fig. 5.

Werthamer *et al.*[6] have calculated the components of the Raman tensor for two-phonon scattering from solid argon at $T=0$, $V=22.6$ cm^3/mole. In these calculations the Raman-scattering matrix elements were calculated within the framework of the point-dipole model in which the solid is treated as a collection of neutral but dipole-polarizable point masses. The lattice dynamics were calculated using the harmonic self-consistent phonon theory with the Lennard-Jones 6:12 potential. For a cubic lattice the scattering efficiency can be written

$$S(\nu) = \hat{\epsilon}_f \hat{\epsilon}_i : \underline{S}(\nu) : \hat{\epsilon}_f \hat{\epsilon}_i , \qquad (2)$$

in terms of the fourth-rank tensor $\underline{S}(\nu)$. Here $\hat{\epsilon}_{(i,f)}$ is the unit polarization vector for the incident (i) or scattered (f) light. $\underline{S}(\nu)$ then has the same symmetry properties as the elastic constant tensor, and hence can have no more than three independent elements, which Werthamer *et al.* have called S_{11}, S_{44}, and S_{12} in the usual Voigt notation. Furthermore, because of the model used, the symmetry of the dipole tensor requires that

$$S_{12} = -\tfrac{1}{2} S_{11} . \qquad (3)$$

With these restrictions the expression derived by Werthamer[7] for the two-phonon Raman-scattering efficiency in the point-dipole model becomes

$$\begin{aligned} S(\nu) = {} & S_{11}(\nu)(\hat{\epsilon}_f \cdot \hat{\epsilon}_i)^2 + S_{44}(\nu)[1 - (\hat{\epsilon}_f \cdot \hat{\epsilon}_i)^2] \\ & + [4S_{44}(\nu) - 3S_{11}(\nu)](\epsilon_{fX}\epsilon_{fY}\epsilon_{iX}\epsilon_{iY} \\ & + \epsilon_{fY}\epsilon_{fZ}\epsilon_{iY}\epsilon_{iZ} + \epsilon_{fZ}\epsilon_{fX}\epsilon_{iZ}\epsilon_{iX}) , \end{aligned} \qquad (4)$$

where $\epsilon_{(i,f)\beta}$ denotes the component of $\hat{\epsilon}_{(i,f)}$ along the βth cube axis of the crystal. The elements $S_{11}(\nu)$ and $S_{44}(\nu)$ are given by

$$S_{11,44}(\nu) = \frac{1}{2}\frac{N}{V}\left(\frac{\omega_i}{c}\right)^4 \alpha^4 N^{-1} \sum_{\vec{k}} \sum_{\lambda\lambda'} \left(\frac{\hbar^2}{M^2 \nu_{\vec{k}\lambda} \nu_{\vec{k}\lambda'}}\right) \delta(\nu - \nu_{\vec{k}\lambda} - \nu_{\vec{k}\lambda'}) \left| \sum_{\vec{\tau}} (1 - \cos \vec{k} \cdot \vec{\tau}) [\langle \vec{e}_{\vec{k}\lambda} \vec{e}_{\vec{k}\lambda'} : \nabla\nabla\vec{\mathrm{T}}(\vec{\tau}) \rangle]_{XX,XZ} \right|^2 , \qquad (5)$$

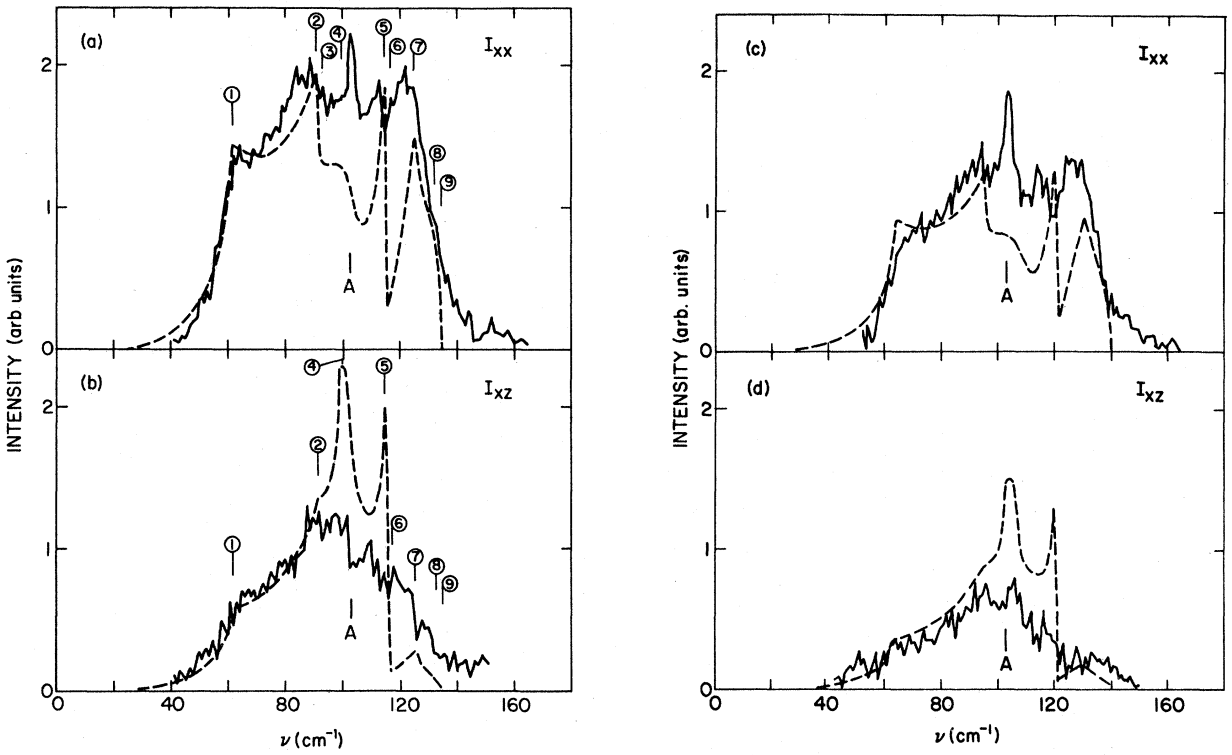

FIG. 5. Low-temperature solid-argon spectra with background subtracted and with polarization analysis performed (see text). (a), (b) 19 K, 22.6 cm^3/mole; (c), (d) 14 K, 22.0 cm^3/mole. Solid lines are experimental curves obtained from the raw data in Fig. 4 as described in the text. Dashed curves are calculated results from Ref. 6. The numbers refer to various features of the calculated curves and are as follows: (1) $2(\frac{1}{2},\frac{1}{2},\frac{1}{2})_T$; (2) $2(1,\frac{1}{2},0)_T$; (3) $2(1,0,0)_T$; (4) $(\frac{1}{2},\frac{1}{2},\frac{1}{2})_L + (\frac{1}{2},\frac{1}{2},\frac{1}{2})_T$; (5) $2(1,\frac{1}{2},0)_L$; (6) $2(0.58,\ 0.58,0)_L$; (7) $2(0.81,\ 0.25,\ 0.25)_L$; (8) $2(\frac{1}{2},\frac{1}{2},\frac{1}{2})_L$; (9) $2(1,0,0)_L$. Dashed curves in (c), (d) were obtained from those in (a), (b) by scaling all frequencies by 1.04 and by changing the intensity (see text). *A* indicates laser fluorescence line.

where the crystal has N atoms in volume V, each with polarizability α and mass M, and ω_i is the angular frequency of the incident light. The crystal phonons have frequencies $\nu_{\vec{k}\lambda}$ and polarization vectors $\vec{e}_{\vec{k}\lambda}$ characterized by wave vector $\vec{k}$ in the first zone and branch index λ. The tensor $\vec{\vec{T}}(\vec{\tau})$ has the dipolar form

$$\vec{\vec{T}}(\vec{\tau}) = \frac{\vec{\vec{1}}}{\tau^3} - \frac{3\vec{\tau}\vec{\tau}}{\tau^5}\,, \tag{6}$$

where the vectors $\vec{\tau}$ connect mean atomic sites in the crystal. The brackets denote an average over the phonon zero-point motion. (Notation and equations based on Ref. 6.) Thus, in this model, the electron-phonon interaction is manifested only through the dipole-dipole interaction involving the individual atomic polarizabilities α.

For a polycrystal, Eq. (4) reduces to

$$S(\nu)|_{\text{poly}} = \tfrac{3}{5}[\tfrac{1}{2}S_{11}(\nu) + S_{44}(\nu)][1 + \tfrac{1}{3}(\hat{\epsilon}_i \cdot \hat{\epsilon}_f)^2]\,, \tag{7}$$

so for a polycrystal the I_{XX} and I_{XZ} spectra should be related by a simple scale factor. Inspection of Fig. 5 shows immediately that this is not the case for the present samples, indicating that the samples had a single grain or possibly several similarly oriented grains in the scattering volume. Since this region was only about 0.3 cm long and less than 100 μm in diameter such a situation would indeed by quite likely. Careful analysis shows that the best fit to the present data is obtained under the assumption that the crystallographic-cube axes lie along the laboratory (X, Y, Z) axes so that cross terms in Eq. (4) do not contribute (actually a misorientation from this configuration of 15°–20° in any direction produces results which differ but little and would give equally good fits to the data). If the crystals in fact have this orientation then we should have $I_{XX}(\nu) \propto S_{11}(\nu)$ and $I_{XZ}(\nu) \propto S_{44}(\nu)$.

The functions $S_{11}(\nu)$ and $S_{44}(\nu)$ calculated by Werthamer *et al.*[6] are shown in Fig. 5 where they have been scaled in amplitude to give rough agreement with the data. The same scale factor has been applied to both S_{11} and S_{44}. The functions are

also plotted in Fig. 5 for the 22.0-cm^3/mole sample. In this case a different amplitude scale factor has been used (but again the same for S_{11} and S_{44}) and the frequencies have been increased by a factor of 1.04 to provide approximate agreement with this higher-density data. It should be noted that the calculated spectra refer to $T=0$, while the measured spectra were obtained at somewhat higher temperatures. The low-frequency portions of the calculated spectra should in principle be increased slightly to correspond to these temperatures, but this small correction has not been made in Fig. 5.

Nearly all the prominent features seen in the calculated spectra are present in the measured spectra as well. An exception is the strong peak in $S_{44}(\nu)$ around 100 cm^{-1} (for the 22.6-cm^3/mole sample). According to the published calculations, this peak results in part from contributions near the point $[(1,0,0)_L+(\frac{1}{2},\frac{1}{2},\frac{1}{2})_T]$ in the calculated joint density of states. However, this point is not at $q=0$ and should therefore not be present in the two-phonon Raman spectra. Thus, this peak may represent an error in the original calculations.

The model calculations give a particularly good representation of the low-frequency part of the spectrum (below ~95 cm^{-1}), reproducing both the shapes and relative amplitudes of $I_{XX}(\nu)$ and $I_{XZ}(\nu)$ quite well in this region. The agreement at higher frequencies is less satisfactory. Although the main features seem to correspond qualitatively, the widths and intensities (relative to the low-frequency data) are not given adequately by the calculations, and the observed peaks are at somewhat lower frequency than the calculated ones.

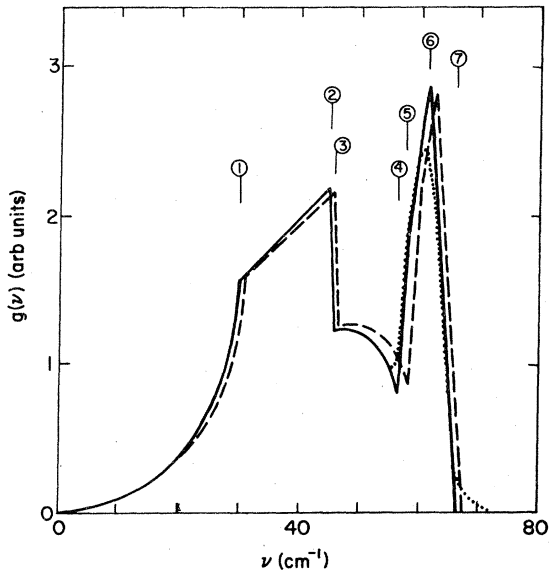

FIG. 6. Density-of-states calculations for solid argon. Solid-line—harmonic model, accurate potential (Ref. 9); dotted line—anharmonic model, accurate potential (Ref 10); dashed line—self-consistent harmonic model, Lennard-Jones potential (Ref. 6). Numbered features are as follows (Ref. 6): (1) $(\frac{1}{2},\frac{1}{2},\frac{1}{2})_T$; (2) $(1,\frac{1}{2},0)_T$; (3) $(1,0,0)_T$; (4) $(1,\frac{1}{2},0)_L$; (5) $(0.58,0.58,0)_L$; (6) $(0.81,0.25,0.25)_L$; (7) $(1,0,0)_L$.

One obvious difference between these two portions of the spectrum is that the low-frequency part is dominated by the transverse modes while the higher frequency behavior is determined primarily by the longitudinal modes. Comparisons between the calculated and measured Brillouin spectra for solid krypton[8] have indicated that this point-dipole model does not correctly predict the ratio of transverse to longitudinal-mode light-scattering intensity for the small q modes involved there; the present results shown in Fig. 5 indicate that this ratio is not given accurately for the large q modes either.

Other discrepancies between the calculated and measured spectra in Fig. 5 can probably be attributed to the fact that the Lennard-Jones potential is not an accurate representation of the argon-argon interactions, and to the fact that anharmonic effects are not properly treated in the calculations. An indication of the extents of these two contributions can be had by comparing the frequency distribution $g(\nu)$ calculated by Werthamer *et al.*[6] using their Lennard-Jones model (the same model used for the spectra in Fig. 5) with the $g(\nu)$ calculated by Cohen and Klein[9] using an accurate argon-argon potential.[10] This latter calculation was made both with and without including anharmonic effects. These various calculations are compared in Fig. 6. The main contributions of anharmonicity appear to be a rounding of the valley near 55 cm^{-1}, a rounding and shift to lower frequencies of the peak near 60 cm^{-1}, and a pronounced high-frequency tail above the harmonic cutoff. The Lennard-Jones potential used by Werthamer *et al.* resulted in a slight shift of the entire spectrum to higher frequencies in comparison with the results with the more accurate potential. This shift is relatively greater for the region between 50 and 65 cm^{-1} than for the remainder of the frequency range.

Based on these considerations one can estimate how the calculated $S_{11}(\nu)$ and $S_{44}(\nu)$ would be changed if a more accurate potential were used and if anharmonic effects were included in the calculation. In the first place, an accurate potential would cause all features of the calculated spectra to be shifted to lower frequencies. The largest shifts would occur for features 5–7 (Fig.

5) which would shift down in frequency by 3–4 cm^{-1}. This would bring the location of these features into excellent agreement with the corresponding features in the experimental spectra. Anharmonic effects would be expected to cause significant broadening of peak 5 and rounding of valley 6, in agreement with the observed spectra. Anharmonic effects would also be expected to introduce a tail extending above the harmonic high-frequency cutoff to about 145 cm^{-1} (for the 22.6-cm^3/mole sample), again in excellent agreement with the observed behavior. It appears that if the argon lattice dynamics were treated correctly by using an accurate potential and properly including anharmonic effects, then the only differences between the calculated and observed spectra would lie in the relative intensities of light scattered from longitudinal and transverse modes. [This statement assumes that the pronounced feature 4 in the calculated $S_{44}(\nu)$ spectrum is a computational error as discussed above.] Since absolute intensities were not measured, no conclusions about the accuracy of absolute intensities predicted by the point-dipole model can be drawn from this experiment. Other calculations and measurements have shown this model to be seriously in error on absolute intensity prediction, however.[11]

IV. TEMPERATURE DEPENDENCE

For a sample constrained to constant density, the lattice frequencies usually do not change appreciably with temperature. In this case the two-phonon spectra at high temperatures should be given reasonably well by the low-temperature spectra weighted by the occupation numbers of the phonons involved. [In a correct calculation of the high-temperature spectra resulting from this model the angular brackets $\langle\ \rangle$ in Eq. (5) should now be interpreted to mean a thermal average at the temperature in question, and this may change the relative weighting of different portions of the spectrum.] If the phonons i, j produce two-phonon sum and difference spectra described, respectively, by $S_{xx}(\nu_i, \nu_j)$, $S_{xz}(\nu_i, \nu_j)$, and $D_{xx}(\nu_i, \nu_j)$, $D_{xz}(\nu_i, \nu_j)$ and if these quantities are not strongly temperature dependent then at any temperature the complete spectra should be given by

$$I_{XX,\,XZ}(\nu, T) = \frac{1}{2}\sum_{i,j} S_{XX,\,XZ}(\nu_i, \nu_j)[\bar{n}(\nu_i, T)+1][\bar{n}(\nu_j, T)+1]\delta(\nu_i+\nu_j-\nu) + \sum_{i,j} D_{XX,\,XZ}(\nu_i, \nu_j)[\bar{n}(\nu_i, T)+1][\bar{n}(\nu_j, T)]\delta(\nu_i-\nu_j-\nu)\,, \tag{8}$$

where

$$\bar{n}(\nu_i, T) = [\exp(h\nu_i/kT) - 1]^{-1}\,, \tag{9}$$

is the average occupation number for a phonon of frequency ν_i. Since $\bar{n}(\nu_i, 0) = 0$ the low-temperature spectra are just

$$I_{XX}(\nu, o) = \frac{1}{2}\sum_{i,j} S_{XX}(\nu_i, \nu_j)\delta(\nu_i+\nu_j-\nu)\,,$$
$$I_{XZ}(\nu, o) = \frac{1}{2}\sum_{i,j} S_{XZ}(\nu_i, \nu_j)\delta(\nu_i+\nu_j-\nu)\,. \tag{10}$$

Without doing a complete calculation, one can indicate the nature of the changes expected at finite temperature due to changes in phonon occupation number by introducing the approximations

$$I^{\text{sum}}_{XX}(\nu, T) \cong I_{XX}(\nu, 0)[\bar{n}(\tfrac{1}{2}\nu, T)+1]^2\,,$$
$$I^{\text{sum}}_{XZ}(\nu, T) \cong I_{XZ}(\nu, 0)[\bar{n}(\tfrac{1}{2}\nu, T)+1]^2\,. \tag{11}$$

Spectra measured for the 22.0-cm^3/mole sample at $T = 60$ K and at $T = 153.5$ K are shown in Figs. 7 and 8, respectively. The data shown have been corrected for background and converted to $I_{XX}(\nu, T)$ and $I_{XZ}(\nu, T)$ by the procedure which was described above for the low-temperature data. Also shown in the figures are two-phonon sum spectra calculated from Eq. (11) and the experimental low-temperature data shown in Fig. 5. [Equations (11) were used as well to correct for the nonzero temperatures at which the data of Fig. 5 were obtained.] It was necessary to divide the results of Eqs. (11) by factors of 1.2 and 5.0 in order to approximately reproduce the measured intensities at $T = 60$ K and $T = 153.5$ K, respectively, and it is these arbitrarily scaled "calculated" two-phonon spectra which are shown in Figs. 7 and 8.

For $T = 60$ K these calculated spectra reproduce the shapes of the measured $I_{XX}(\nu, T)$ and $I_{XZ}(\nu, T)$ spectra and the ratio $I_{XZ}(\nu, T)/I_{XX}(\nu, T)$ quite well for $\nu > 65$ cm^{-1}. The measured spectra do indicate some additional "smearing" of the features associated with the longitudinal modes, consistent with the known decrease of the lifetimes of these phonons with increasing temperature.[12] No contributions from the two-phonon difference spectra are expected above about 70 cm^{-1} which

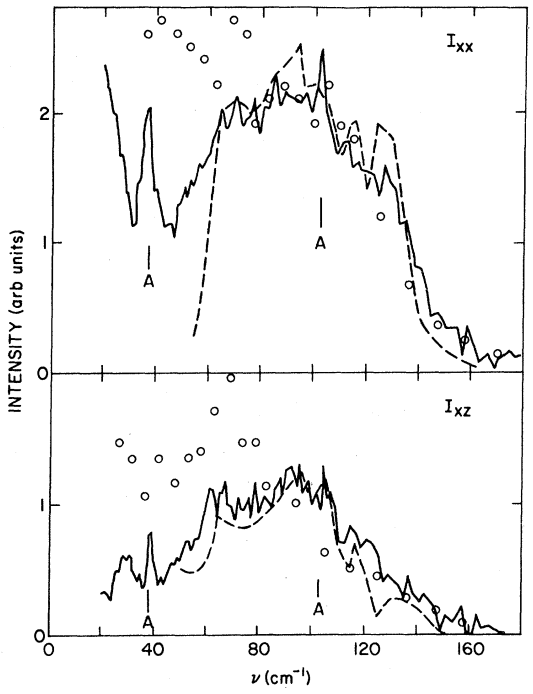

FIG. 7. Solid-argon spectra at 60 K, 22.1 cm^3/mole measured with triple monochromator. Background has been subtracted and polarization anaylysis performed as described in the text. Solid line—experimental results; dashed line—approximation two-phonon sum contribution (see text); circles—calculations of Ref. 13 scaled as described in text. *A* indicates laser fluorescence line.

is the maximum lattice frequency at this density. However, the extra intensity in the measured spectra at frequencies below 65 cm^{-1} can probably be attributed to these difference spectra. This could be readily tested by a calculation within the framework of the point-dipole model.

Alder *et al.*[13] have calculated Raman-scattering band profiles for solid argon at several densities at high temperatures. These were molecular dynamics calculations using the Lennard-Jones potential and a point-dipole model. One set of these calculated spectra correspond to a temperature of 61.2 °K and a molar volume of 23.71 cm^3/mole (i.e., a point along the vapor pressure curve). The lattice frequencies at a molar volume of 22.0 cm^3/mole at which the experimental spectra in Fig. 7 were measured should be approximately 25% larger than at the point where these spectra were calculated. Because of the temperature factors [see Eq. (8) for example] a direct scaling of the calculated spectra for comparison with the experimental spectra is not really appropriate. However, at 60 K these temperature factors are not too large and such a scaling may not be too unreasonable. Therefore, those calculated spectra with their frequencies increased by a factor of 1.25 are also shown in Fig. 7. Intensities have been adjusted to give rough agreement with the measured I_{XX} at 80–100 cm^{-1}, with the same scale factor being used for I_{XX} and I_{XZ}. This agreement is reasonably good considering the approximations involved in these adjustments. It does appear that these calculated spectra weight the transverse modes too heavily relative to the longitudinal modes, which is consistent with the results found above for the point-dipole model at low temperatures. The calculated spectra also seem to have too much intensity below about 50 cm^{-1}, the range where the difference spectra predominate. This may be due to a failure of the scaling approximations made for this comparison or may also reflect a failure of the point-dipole model or a breakdown of the classical mechanics implicit in these calculations.

At 153.5 K, all sharp features have been eliminated from the measured spectra. Comparison of Figs. 5, 7, and 8 indicates that the spectra at this high temperature are determined primarily by the phonon occupation numbers $\bar{n}(\nu, T)$. A wide

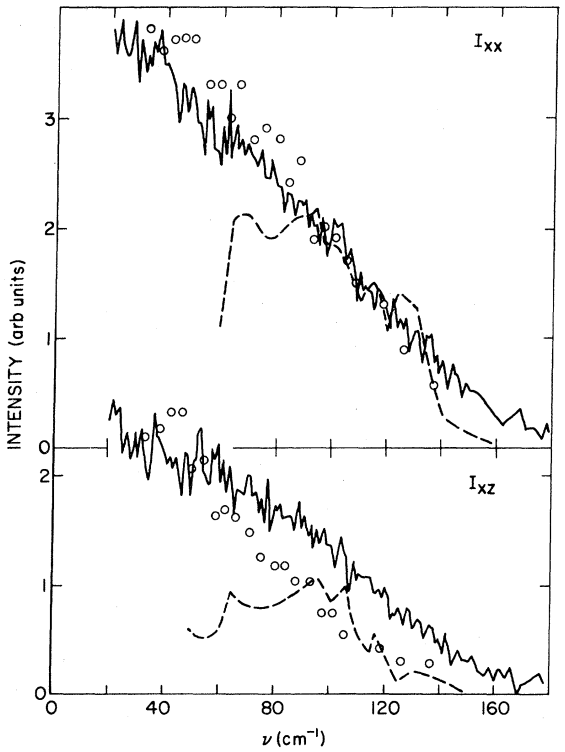

FIG. 8. Solid-argon spectra at 153.5 K, 22.3 cm^3/mole, measured with triple monochromator. Solid line—experimental results; dashed—approximate two-phonon sum contributions (see text); circles—calculations of Ref. 13 (not scaled).

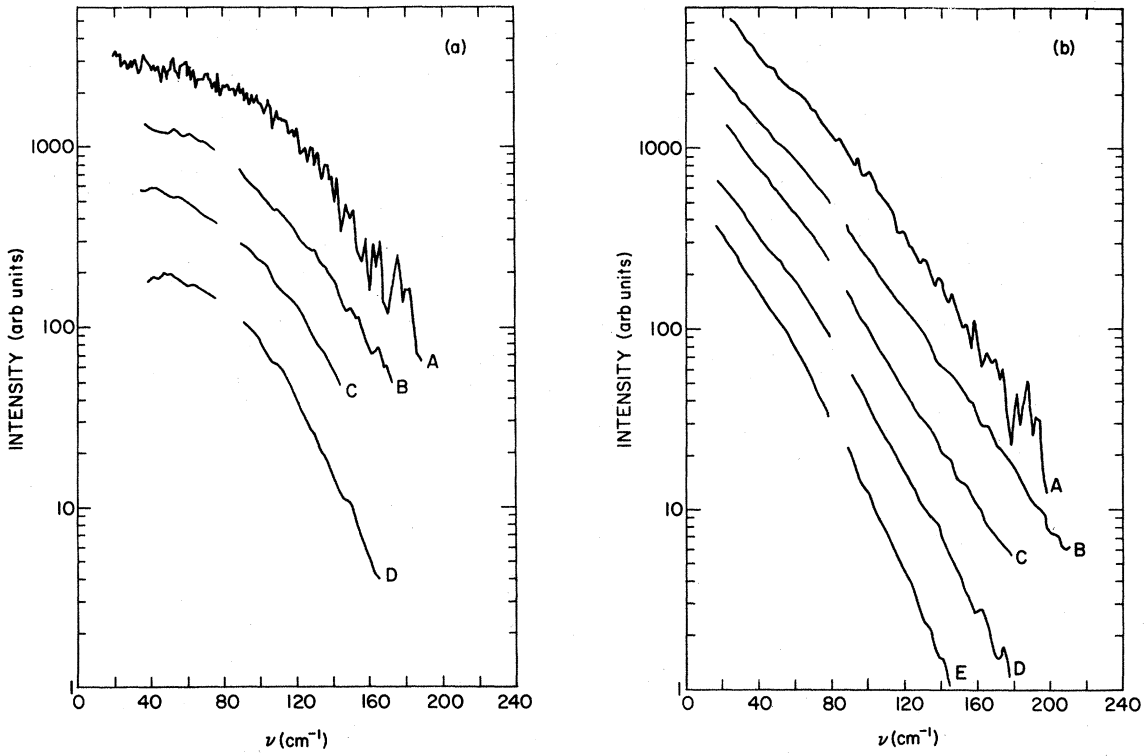

FIG. 9. (a) Solid-argon depolarized spectra at points along the melting curve. (A) 153.5 K, 22.3 cm^3/mole (T_m = 166 K); (B) 140 K, 22.95 cm^3/mole (T_m=144 K); (C) 128 K, 23.44 cm^3/mole (T_m= 128 K); (D) 108 K, 24.05 cm^3/mole (T_m=108 K). (b) Fluid-argon depolarized spectra at points along the melting curve. (A) 166 K; 24.14 cm^3/mole (T_m=163 K); (B) 150 K, 24.53 cm^3/mole (T_m=150 K); (C) 128 K, 25.47 cm^3/mole (T_m=128 K); (D) 110 K, 26.71 cm^3/mole (T_m=105 K); (E) (90 K, 27.96 cm^3/mole (T_m=86 K). T_m is the melting temperature of solid or fluid argon at the specified molar volume. The spectra A were obtained with the triple monochromator, while all other spectra were obtained with the double monochromator. Backgrounds have been subtracted in all cases.

variety of low-temperature spectra $I_{XX}(\nu, 0)$ and $I_{XZ}(\nu, 0)$ would give rise to quite similar results when used to calculate high-temperature spectra according to Eq. (11).

Alder *et al.*[13] also used molecular dynamics and the point-dipole model to calculate spectra at a point which corresponds to 144 K, 23.07 cm^3/mole for argon. These spectra are shown in Fig. 8 where the intensities have been normalized to give approximate agreement with the experimental spectra at 153.5 K, 22.35 cm^3/mole (the same normalization factor again being used for both I_{XX} and I_{XZ}). The small discrepancies in slope can probably be accounted for by the temperature and molar volume differences between the experimental conditions and those of the calculations, although some of these discrepancies may also be due to the incorrect relative weighting of transverse and longitudinal modes as discussed above.

Both the 60-K spectra and the 153.5-K spectra show some "extra" intensity at frequencies above the two-phonon cutoff. This may be due to three-phonon or still higher-order processes. The frequency dependence at high frequencies (above 120–140 cm^{-1}) appears to be approximately exponential for all high-temperature spectra measured [see Fig. 9(a) for some examples], but the statistical accuracy and the uncertainties in background subtraction are such that it is difficult to establish this behavior with certainty.

The fact that the intensities measured at high temperatures were less than predicted by a simple scaling of the low-temperature data by Eq. (11) is probably an experimental artifact. This behavior was observed in all solid samples studied, but differed quantitatively from sample to sample. The intensities measured for liquid samples near the melting curve were much more nearly in agreement with this simple scaling.

V. FLUID AND SOLID NEAR MELTING

Fleury *et al.*[14] observed strong similarities between the liquid and solid Raman spectra for

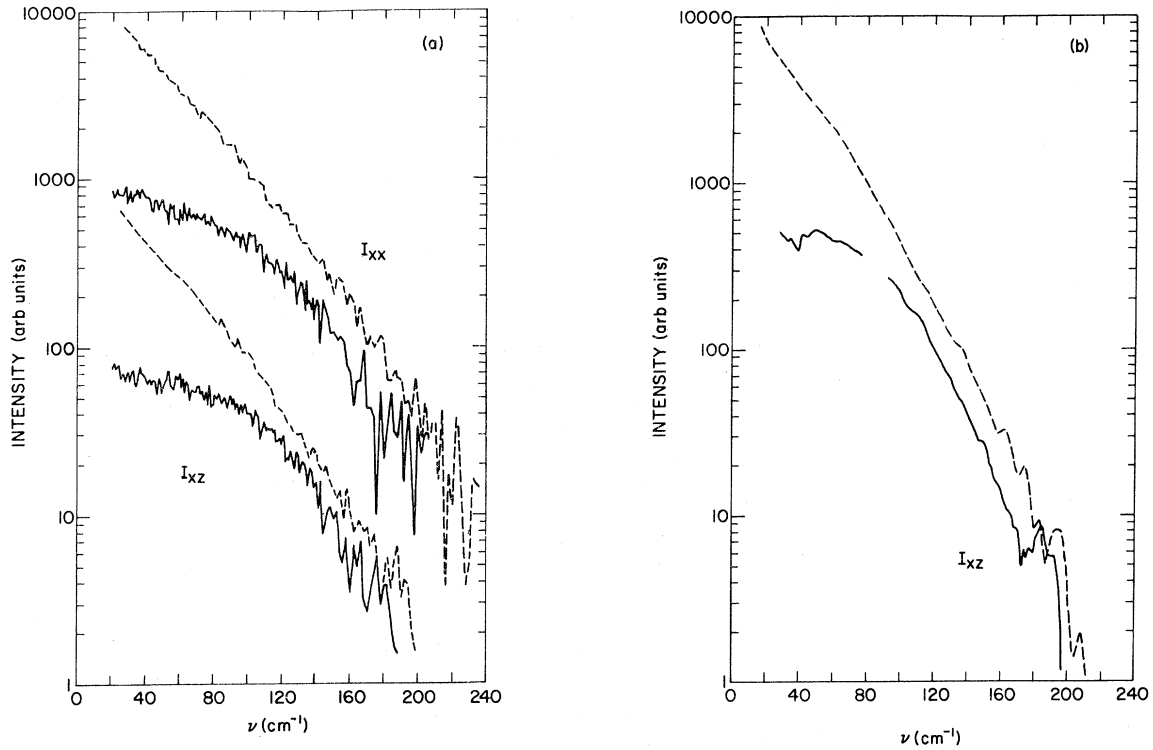

FIG. 10. Comparison of solid and fluid argon near the melting curve. (a) $T_m \sim 165$ K; (b) $T_m \sim 106$ K. Spectra are the same as shown in Fig. 9. Dashed line—fluid; solid line—solid.

the noble gases near their respective triple points. In the present experiment spectra have been measured for solid and fluid argon at similar temperatures and pressures at several high-pressure points along the melting curve. These measurements spanned the range 90–168 K (0.2–4.2 kbar). The third monochromator was not used for most of these measurements, and since there appeared to be little polarization dependence to the band shapes [cf. Fig. 10(a)], only the depolarized spectra were measured at most points. The density dependence of these liquid and solid spectra are shown in Fig. 9 and a comparison between the liquid and solid band shapes is made in Fig. 10. The spectral shapes near the triple point are in excellent agreement with those observed by Fleury *et al.* The similarities between fluid and solid spectra observed by Fleury *et al.* are seen to persist to the highest pressures studied. Above some frequency ν_2 (~ 100 cm^{-1}) the spectra appear to be exponential with the same exponent for fluid and solid. Below ν_2 the solid spectra become much less dependent on frequency ν. Below ν_1 the fluid spectra appear to change to an exponential with a different slope. Following Fleury *et al.*[15] we write the fluid spectra

$$I = I_0 e^{-\nu/\Delta_1}, \quad \nu < \nu_1 ,$$
$$I = I_0 e^{-\nu/\Delta_2}, \quad \nu_1 < \nu . \tag{12}$$

The variations of ν_1, ν_2, Δ_1, and Δ_2 along the melting curve are shown in Fig. 11.

The observed solid and fluid band shapes at a given pressure differ only at frequencies below $\nu_2 \approx 100$ cm^{-1}. The absence of long-range order in the liquid will lead to a destruction of the momentum selection rules so that a "disorder-induced" first-order Raman spectrum is to be expected for the liquid in the spectral region up to about 70–80 cm^{-1}. On the other hand, it is well known that in the solid phase long-range order persists up to the melting point, so that the solid phase near melting should exhibit no first-order (i.e., one-phonon) Raman scattering (actually a very weak first-order spectrum may be present due to defects in the crystalline solid structure). Thus it is possible that most of the differences between solid and liquid band shapes in the spectral region studied here could be accounted for by differences in selection rules between the two phases, and that no great differences in the dynamical responses of the two phases would be required to explain the observed spectra.

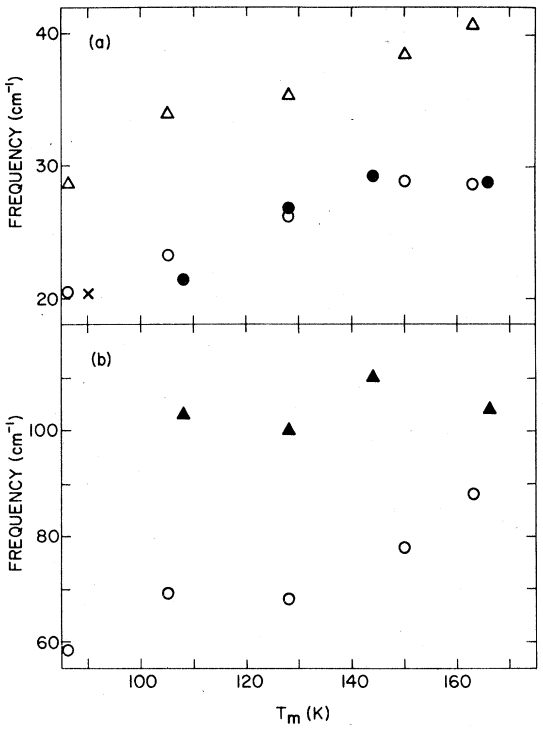

FIG. 11. Variation of spectral features along the melting curve. (a) △—low-frequency exponent Δ_1 for fluid; o-high-frequency exponent Δ_2 for fluid; ●—high-frequency exponent Δ_2 for solid; ×—high-frequency exponent Δ_2 for fluid from Ref. 14. (b) o—"knee" ν for fluid; △—"knee" ν_2 for solid.

Fleury *et al.*[15] also measured spectral shapes of a number of dense fluid argon samples at 180 and 300 K. For these samples the spectra were also well described by simple exponentials with one slope at low frequencies and a different slope at high frequencies. However, for all their fluid-argon samples they found Δ_1 (low frequencies) to be less than Δ_2 (high frequencies) while for all the present spectra along the melting curve Δ_1 is greater than Δ_2. Molecular dynamics calculations of Alder *et al.*[16] for the Lennard-Jones fluid in the point-dipole model show that both types of behavior can be observed under appropriate conditions, but unfortunately these calculations cannot be directly related to the temperatures and molar volumes at which the present measurements were made. (Fleury *et al.* found Δ_1 greater than Δ_2 for their fluid neon samples, in contrast to their fluid argon data.) Measurements in the fluid at temperatures and densities linking the present experimental range with that of Fleury *et al.* should show a transition between these two types of behavior, and would thus be most interesting.

VI. SUMMARY

The point-dipole model is seen to provide a reasonably good representation of the band shapes and relative intensities of the two-phonon-sum I_{XX} and I_{XZ} Raman spectra in solid argon at low temperatures. Plausibility arguments indicate that many of the discrepancies between the calculated and observed spectra would disappear if an accurate argon-argon potential and a proper anharmonic treatment of the argon dynamics were included in the calculations. The point-dipole model does not seem to give a correct representation of the relative scattering strengths of transverse and longitudinal modes however.

At higher temperatures this latter problem is still apparent in the point-dipole-model calculations. In addition there is a large discrepancy between the calculated and experimental two-phonon-difference spectra. Further calculations will be required to determine the source of this discrepancy. At high temperatures the observed band shapes are seen to be dominated by the phonon-occupation factors, although some smoothing of spectral features due to anharmonic effects is apparent as well.

The similarities between fluid and solid band shapes near melting, previously observed only at low pressures, are seen to persist to much higher pressures. However, direct comparison between solid and fluid spectra is not very helpful in understanding the dynamical differences between the two phases, because the selection rules are different in the two phases and because the spectral shapes are dominated by the large Bose distribution factors $\bar{n}(\nu)$. Fluid spectra near the melting curve are found to be qualitatively different from those previously observed far from melting, and further experiments and/or calculations to observe this changeover in behavior would be interesting.

ACKNOWLEDGMENTS

One of the authors (R.K.C.) would like to thank Professor R. O. Simmons for his support during this project. Dr. L. A. Schwalbe also provided valuable assistance during the early phases of the research. This work was performed under the auspices of the Dept. of Energy at Argonne and supported by Dept. of Energy Grant DOE EY-76-C-02-1198 at the University of Illinois and by the NSF under Grant No. NSF DMR-76-01058.

APPENDIX: POLARIZATION EFFECTS FROM PRESSURE-CELL WINDOWS

Consider a plane-parallel slab of uniaxial material of thickness d with the optical axis perpen-

dicular to the slab surface. Assume the media on both sides of this slab are isotropic and described by indices of refraction n_i and n_f, respectively. Let the slab material be described by refractive indices n_0 for the ordinary ray and n_e for an extraordinary ray traveling perpendicular to the optical axis. A ray with incident angle θ_i will split into an ordinary ray and an extraordinary ray. The normals to the wave fronts for these two rays will make angles θ_o and θ_e, respectively, with the optical axis. After transversing the slab the rays can recombine to form a single ray traveling at an angle θ_f to the slab normal, but because of different paths and different velocities for the two rays within the slab there will be a phase differences δ between them when they recombine. A standard analysis (Born and Wolf,[17] Chap. 14) gives

$$n_i \sin\theta_i = n_o \sin\theta_o = n_f \sin\theta_f = n \sin\theta_e , \tag{A1}$$

$$\delta = (2\pi d/\lambda)(n_o \cos\theta_o - n \cos\theta_e) , \tag{A2}$$

$$1/n^2 = \sin^2\theta_e/n_e^2 + \cos^2\theta_e/n_o^2 . \tag{A3}$$

In the limit of small angles it can be shown from these equations that

$$\delta \approx (n_i^2/n_o)\theta_i^2(\pi d/\lambda)(n_o^2/n_e^2 - 1) . \tag{A4}$$

For sapphire $n_o = 1.768$, $n_e = 1.760$,[18] while n_i ~1–1.5 for most media, so

$$\delta \sim (0.016 \text{ to } 0.036)(d/\lambda)\theta_i^2 .$$

For the conditions of the present experiment $\lambda \sim 5000$ Å and $d = 0.3$ cm, so

$$\delta \sim (1.7 \text{ to } 3.8)\theta_i^2 , \tag{A4'}$$

for θ_i and δ now given in degrees, the two coefficients corresponding to $n_i = 1.0$ and 1.5, respectively.

A straightforward analysis using Eqs. (A1)–(A3) and the usual electromagnetic boundary conditions (cf. Ref. 17) leads to an expression for the intensity I_{Xf} measured with an X-oriented polarization analyzer after transmission through a window with its optic axis along the Z axis and normal to its surfaces (cylindrical symmetry and perfect transmission at the interfaces are assumed)

$$I_{Xf} \cong I_{Xi} \frac{\frac{3}{4}\int(1 + \frac{1}{3}\cos\delta)\sin\theta d\theta}{\int \sin\theta d\theta} + I_{Yi} \frac{\frac{1}{4}\int(1 - \cos\delta)\sin\theta d\theta}{\int \sin\theta d\theta} , \tag{A5}$$

with a similar expression for I_{Yf}. Here I_{Xi} and I_{Yi} are the corresponding intensities which would be observed with the same aperature but with the window absent, θ is the inclination between a given ray and the optical axis, and the integrals extend over all values of θ in the beam of interest.

In the present experiment the incident laser beam is focused by a lens with ~ 15-cm focal length so $\theta < 2°$ and $\delta < 8°$. In this case $I_{Xf} \approx I_{Xi}$; $I_{Yf} \approx I_{Yi}$, so there will be no appreciable polarization mixing in the incident beam under these conditions. For the Raman-scattered light, the collecting aperature is considerably larger, with values of θ_i up to ~ 20°. Inspection of (A4′) indicates that for values of θ_i up to 20°, values of δ up to 1500° are possible. Hence cos δ will go through many oscillations when (A5) is integrated over θ, and the terms containing cos δ will make negligible contributions to the integrals. Thus in this case we can write

$$I_{Xf} \approx \tfrac{1}{4}(3I_{Xi} + I_{Yi}) , \quad I_{Yf} \approx \tfrac{1}{4}(3I_{Yi} + I_{Xi}) . \tag{A6}$$

The window effects can thus be eliminated by inversion of (A6) to give

$$I_{Xi} = \tfrac{1}{2}(3I_{Xf} - I_{Yf}) , \quad I_{Yi} = \tfrac{1}{2}(3I_{Yf} - I_{Xf}) . \tag{A7}$$

Numerical integrations have shown that the contributions from parts of the sample away from the window symmetry axis do not significantly affect these results.

[1] B. S. Agarwal, R. D. Kirby, and J. R. Hardy, Phys. Rev. B 11, 5153 (1975), and references therein.
[2] S. Go, H. Bilz, and M. Cardona, Phys. Rev. Lett. 34, 580 (1975).
[3] R. K. Crawford and W. B. Daniels, J. Chem. Phys. 50, 3171 (1969).
[4] W. F. Lewis, D. A. Benson, R. K. Crawford, and W. B. Daniels, J. Phys. Chem. Solids 35, 383 (1974).
[5] V. M. Cheng, R. K. Crawford, and W. B. Daniels, Phys. Lett. A 43, 109 (1973).
[6] N. R. Werthamer, R. L. Gray, and T. T. Koehler, Phys. Rev. B 2, 4199 (1970).
[7] N. R. Werthamer, Phys. Rev. 185, 348 (1969).
[8] N. R. Werthamer, Phys. Rev. B 6, 4075 (1972); Y. Kato and B. P. Stoicheff, *ibid.* 11, 3984 (1975).
[9] S. S. Cohen and M. L. Klein, J. Chem. Phys. 61, 3210 (1974).
[10] J. A. Barker, R. A. Fischer, and R. O. Watts, Mol. Phys. 21, 657 (1971); J. M. Parson, P. E. Siska, and Y. T. Lee, J. Chem. Phys. 56, 1511 (1972).
[11] B. J. Alder, J. J. Weis, and H. L. Strauss, Phys. Rev. A 7, 281 (1973).
[12] J. P. Hansen and M. L. Klein, Phys. Rev. B 13, 878 (1976).
[13] B. J. Alder, H. L. Strauss, J. J. Weis, J. P. Hansen, and M. L. Kelin, Physica (Utr.) B 83, 249 (1976).
[14] P. A. Fleury, J. M. Worlock, and H. L. Carter, Phys. Rev. Lett. 30, 591 (1973).

[15]P. A. Fleury, W. B. Daniels, and J. M. Worlock, Phys. Rev. Lett. 27, 1493 (1971).
[16]B. J. Alder, H. L. Strauss, and J. J. Weis, J. Chem. Phys. 59, 1002 (1973).
[17]M. Born and E. Wolf, *Principles of Optics*, 5th ed. (Pergamon, New York, 1975), Chap. 14.
[18]T. A. Davis and K. Vedam, J. Appl. Phys. 38, 4555 (1967).